HHS Public Access

Author manuscript

Nat Chem. Author manuscript; available in PMC 2015 August 01.

Published in final edited form as:

Nat Chem. 2015 February ; 7(2): 130–139. doi:10.1038/nchem.2133.

Quantitative mapping of zinc fluxes in the mammalian egg reveals the origin of fertilization-induced zinc sparks

Emily L. Que[1], **Reiner Bleher**[1,2], **Francesca E. Duncan**[3], **Betty Y. Kong**[3], **Sophie C. Gleber**[4], **Stefan Vogt**[4], **Si Chen**[4], **Seth A. Garwin**[1,5], **Amanda R. Bayer**[1,5], **Vinayak Dravid**[2,5,6], **Teresa K. Woodruff**[1,3,7,*], and **Thomas V. O'Halloran**[1,5,7,*]

[1]The Chemistry of Life Processes Institute, Northwestern University, Evanston, IL 60208, USA

[2]Northwestern University Atomic and Nanoscale Characterization Experimental Center, Evanston, IL 60208, USA

[3]Department of Obstetrics and Gynecology, Northwestern University, Feinberg School of Medicine, Chicago, IL 60611, USA

[4]X-ray Science Division, Argonne National Laboratory, Argonne, IL 60439, USA

[5]Department of Chemistry, Northwestern University, Evanston, IL 60208, USA

[6]Department of Materials Science and Engineering, Northwestern University; Evanston, IL 60208, USA

[7]Department of Molecular Biosciences, Northwestern University, Evanston, IL 60208, USA

Abstract

Fertilization of a mammalian egg induces a series of 'zinc sparks' that are necessary for inducing the egg-to-embryo transition. Despite the importance of these zinc efflux events little is known about their origin. To understand the molecular mechanism of the zinc spark we combined four physical approaches to resolve zinc distributions in single cells: a chemical probe for dynamic live-cell fluorescence imaging and a combination of scanning transmission electron microscopy with energy dispersive spectroscopy, X-ray fluorescence microscopy, and 3D elemental tomography for high resolution elemental mapping. We show that the zinc spark arises from a system of thousands of zinc-loaded vesicles, each of which contains, on average, 10^6 zinc atoms. These vesicles undergo dynamic movement during oocyte maturation and exocytosis at the time of fertilization. The discovery of these vesicles and the demonstration that zinc sparks originate from

Corresponding Authors: Thomas V. O'Halloran, Ph.D., Director, Chemistry of Life Processes Institute, Northwestern University, 2170 North Campus Drive, Silverman 4611, Evanston, IL 60208, Phone: 847-644-9410, Fax: 847-467-1566, t-ohalloran@northwestern.edu, and, Teresa K. Woodruff, Department of Obstetrics and Gynecology, Northwestern University Feinberg School of Medicine, 303 East Superior Street, Lurie 10-121, Chicago, IL 60611, Phone: 312-503-2503, Fax: 312-503-0219, tkw@northwestern.edu.

Author contributions

ELQ, RB, FED, BYK, VPD, TKW, and TVO designed the research. ELQ, RB, FED, BYK, SAG, and ARB performed the research. SCG, SV, and SC helped design and implement XFM experiments and process and analyze data. ELQ, RB, FED, TKW, and TVO wrote the manuscript. All authors discussed the results and commented on the manuscript.

them provides a quantitative framework for understanding how zinc fluxes regulate cellular processes.

The Zn^{2+} ion is well known as an important metalloprotein cofactor that is tightly regulated by cells.[1–4] Unlike other essential divalent metal ions such as Mg^{2+} and Ca^{2+}, Zn^{2+} is typically bound with high affinity (i.e. $K_d < 10^{-12}$) in the catalytic active site of metalloenzymes or in catalytically inactive sites of proteins involved in regulation, transcription and translation. Recently, extraordinary cell-driven changes in the total intracellular Zn^{2+} content have been identified as key events regulating the cell cycle in the mammalian egg: zinc influx is essential during maturation in the 16 hours before fertilization and zinc efflux is essential for embryo formation in the two hours following fertilization.[5–12] These results indicate that zinc fluctuations are serving an instructive or regulatory role in controlling cell cycle progression at the earliest stage of embryonic development. Our goal is to understand the molecular mechanisms of how cells use zinc fluxes to make major decisions.

The female reproductive cells in the mouse have many advantageous properties for probing how cells use inorganic chemistry to control decision-making processes. First, immature mouse oocytes are readily isolated and the entire process of their maturation into an egg and the subsequent conversion into an embryo upon fertilization by a sperm cell all transpires in ca. 48 hours. Three key intermediary stages are well known and progression is controlled by biological checkpoints. Female reproductive cells found within the ovary are arrested in prophase of meiosis I and are called germinal vesicle (GV) oocytes. During meiotic maturation, the GV oocyte exits from prophase I arrest and progresses for 12–16 hours until it stops and arrests in metaphase of meiosis II, at which point the reproductive cell is called an MII egg: this is the first point at which it is competent for fertilization. In the process of maturation, we have shown that the oocyte accrues 20 billion zinc atoms, corresponding to >50% increase in total cellular zinc content, in a time span of several hours.[5] This increase is essential: if zinc accrual is abrogated *in vitro* using a zinc chelator or *in vivo* by acute dietary zinc deficiency, progression to MII and fertilization are significantly impaired.[5,8,11,13] In contrast, fertilization or activation of the MII egg is accompanied by a decrease in total zinc content of ca. 10 billion zinc atoms,[5] as quantified by X-ray fluorescence microscopy (XFM). The loss of zinc at the end of meiosis is necessary to mediate the egg-to-embryo transition as artificial maintenance of high intracellular zinc prevents pronuclear formation.[8] Moreover, treatment of mature eggs with an intracellular zinc chelator leads to a high rate of parthenogenetic activation, or egg activation in the absence of sperm.[6,10] In parthenogenetic activation, early cell division stages of embryogenesis can occur for several days, but a viable embryo does not result. It is not known how these essential fluxes in zinc concentration are controlled at the cellular and molecular levels. Recent studies reveal a plausible path for the uptake of zinc during maturation of the GV oocyte into the MII egg. During maturation, we have identified two abundant zinc transporters in the outer or ooplasmic membrane, namely ZIP6 and ZIP10. These proteins mediate zinc influx during the oocyte-to-egg transition.[14]

In contrast to the uptake in zinc that occurs during maturation, fertilization triggers a series of repetitive efflux events known as “zinc sparks” that release zinc into the extracellular space.[6] Zinc flux during fertilization could involve ion channels, the secretory pathway, or other cellular mechanisms, but a model has not been unequivocally identified. Treatment with parthenogenetic activation agents also induces zinc sparks.[6] Zinc sparks are observed at the cell periphery in a manner that resembles the distribution of zinc in the MII-arrested egg.[6] Based on these observations, we hypothesized that zinc sparks originate from the release of discrete cortical zinc-containing compartments. Other models for the zinc spark are not ruled out by current published results. There are a number of general pathways by which zinc might move from the cytosol into the extracellular space during a zinc spark event. For instance, unidentified orthologs of voltage- and ligand-gated ion channels, ATPase7 family of copper transporters, or other integral membrane proteins including members of the ZnT family of zinc and iron transporters could conceivably facilitate/permit the movement of Zn^{2+} ions.[15–17]

Our ability to distinguish between these models is compromised by the paucity of quantitative physical methods with sufficiently high spatial resolution, with specificity for specific metal ions, and with enough sensitivity to establish metal concentrations in subcellular compartments. As a consequence, zinc has not been monitored throughout an entire biological process in a manner that allows for mass balance analysis of zinc flux in an individual cell, despite the strong evidence that dynamic changes in zinc can regulate key biological decisions. To better address these models for the zinc spark, we developed new chemical tools and applied cutting-edge elemental imaging in single cells to quantitatively determine local changes in the cellular zinc quota before and during fertilization of the mammalian egg. These approaches include the synthesis of a novel zinc-specific probe that can be used at nanomolar concentration for live-cell imaging, scanning transmission electron microscopy with energy dispersive spectroscopy (STEM-EDS) to directly map biological zinc at the ultrastructural level, X-ray fluorescence nanoprobe microscopy to quantify zinc within compartments, and three-dimensional x-ray fluorescence tomography to establish total zinc distribution within the cell. Using these methods together, for the first time we establish that the zinc spark originates from thousands of cortically enriched, zinc-loaded secretory compartments. These vesicles contain ~15% of the total zinc content of the egg and are released from the egg following activation. This vesicular zinc release accounts for the precise loss observed during zinc sparks. Intense interest in putative zinc secretory systems (including those in neurons, pancreatic beta islets, and immune cells)[18–22] has largely utilized qualitative methods to characterize zinc flux. This work provides an unprecedented quantitative demonstration of regulatory fluxes in transition metal content at the single cell level and firmly establishes zinc dependent pathways in meiotic cell cycle regulation in the mammalian egg.

Results

Characterization of the zinc sensor ZincBY-1

Vital fluorogenic zinc sensors facilitate the detection of changes in labile zinc concentration in biological samples.[23–27] We developed a new zinc-sensor, ZincBY-1 (**1**, Figure 1a), with

nanomolar affinity for labile zinc (Figure 1b). Compared to the commercially available zinc sensor FluoZin-3-AM, which requires sensor concentrations up to 10 μM for visualization.[6] ZincBY-1 can be used to highlight zinc in the egg at treatment concentrations as low as 50 nM (Figure 1c), a 200-fold lower concentration than FluoZin-3-AM. In addition, ZincBY-1 does not require AM-ester moieties for cell membrane permeability. As a result, potentially toxic cleavage products of AM-esters (formaldehyde and acetic acid)[28] are not introduced to the cell when ZincBY-1 is utilized.

ZincBY-1 is synthesized from an asymmetric BODIPY core[29,30] and a polypyridine zinc chelator[31] (Figure 1a). The zinc loaded probe has a modest quantum yield (Table S1) and in aqueous buffer, 50 nM ZincBY-1 exhibits a 4.6-fold increase in fluorescence brightness in the presence of zinc (λ_{ex} = 520 nm, λ_{em} = 543 nm) (Figure S1, Table S1). ZincBY-1 displays an apparent zinc dissociation constant of (K_D) of 2.5 ± 0.8 nM (Figures 1b), as determined using EGTA as a competing ligand for zinc (see Supplementary Methods). The fluorescence response is selective for Zn^{2+} over a range of biologically essential metal ions including Ca^{2+}, Mg^{2+}, K^+, and Na^+. Addition of copper ions induces quenching of ZincBY-1 and inhibits the zinc response. This is not surprising, as pyridine-based ligands have previously been shown to have appreciable affinity towards both Cu^{2+} and Cu^+.[32] However this feature of the probe should not affect the utility of this reagent in the egg since copper is an order of magnitude lower in concentration than zinc,[5] and the majority of copper ions are likely to be tightly bound to metalloproteins.[33] The heavy metal ions Hg^{2+} and Cd^{2+} also induce a ZincBY-1 fluorescence increase, however these are not abundant in normal egg cells.[5] Finally, the fluorescence of both apo and Zn-bound ZincBY-1 is not affected by pH changes within the physiologically relevant range (pH 4–8.5) (Figure S1 and Table S1).

In addition to eggs (Figure 1c, described in further detail below), ZincBY-1 can also monitor zinc stores in other cell types, including mouse spermatozoa, a cell known to contain spatially localized zinc.[34–36] Specifically, silver staining following autometallography of fixed sperm identified zinc enrichment within the acrosome.[35] We therefore imaged live sperm with ZincBY-1 as a positive control. Discrete fluorescence was located in the expected acrosomal region of sperm incubated with 50 nM ZincBY-1. Moreover, the fluorescence was quenched after incubation with TPEN (Figure S2). This same location is similarly observed when live sperm are imaged with micromolar amounts of the zinc probes FluoZin-3-AM (Figure S2) and TSQ (experiment performed in hamster sperm).[34]

Spatio-temporal dynamics of labile zinc compartments during meiotic maturation

Oocytes and eggs incubated with 50 nM ZincBY-1 have discrete punctate fluorescent structures that change subcellular localization as a function of meiotic stage. GV oocytes display uniformly distributed punctate structures throughout the cell cortex (Figure 1c-i,ii). MII eggs have a similar staining pattern; however, the distribution was concentrated predominantly in the vegetal hemisphere of the cell, opposite the region where metaphase chromosomes localize (Figure 1c-iv,v). Strikingly, the distribution of labile zinc changed from symmetrical to polarized between the GV to MII stages, mirroring the changes in total zinc distribution observed previously by XFM.[6]

To assess the biological specificity of ZincBY-1, we performed several controls. First, ZincBY-1 fluorescence was abolished by treatment with heavy metal chelator TPEN[37] (Figure 1d), indicating that the signal is due to probe interaction with labile zinc. In addition, punctate peripheral fluorescence was still observed following centrifugation of ZincBY-1 solutions prior to incubation (20 min, 3750 rpm), demonstrating that observed punctate fluorescence is not likely due to cellular uptake of nanoscale aggregates[38] (data not shown). In addition, using Dynamic Light Scattering (DLS) we do not observe aggregates at ZincBY-1 concentrations below 500 nM (Table S2), however we are unable to exclude the possibility that aggregates cannot be detected at these low concentrations. The ZincBY-1 staining pattern in eggs is consistent with that obtained using higher concentrations of other intracellular zinc probes, including FluoZin-3-AM[39] and Zinpyr-4.[40] Both of these probes display hemispherical punctate, cortical fluorescence patterns in the MII egg at concentrations of 5–10 μM (Figure S3, see also Kim 2011). However neither probe provided signal when eggs are treated at 50 nM concentration.

Quantitative analysis of the staining revealed that GV oocytes contained significantly more zinc-rich compartments than MII eggs (9000 ± 200 (N = 36) vs. 8000 ± 300 (N = 30), p = 0.0021) Greater than ~90% of zinc-enriched compartments are localized within 5 microns of the plasma membrane in both cell types (Figure 1e). The small decrease in the number of zinc-enriched compartments associated with meiotic maturation suggests that the compartments are lost in addition to being reorganized during meiotic maturation. We note that while the majority of observed compartments are localized to the egg cortex, small numbers of vesicles are observed throughout the egg, indicating that ZincBY-1 is able to penetrate into the cell (Figure S4). In addition, MII eggs incubated with zinc pyrithione before and after exposure to ZincBY-1 reveals that this fluorescent probe penetrates beyond the cortical region and distributes throughout the egg. (Figure S5). We note that while ZincBY-1 fluorescence can be observed throughout the cell, the probe appears to preferentially localize to intracellular compartments. TPEN controls (Figure 1d) support the zinc-dependence of this localized fluorescence.

The punctate nature of ZincBY-1 staining is consistent with the presence of discrete vesicular compartments that contain high levels of labile zinc; however the cellular components associated with these structures is unknown. We investigated if zinc transporters displayed similar localization as these could be used to facilitate zinc movement in to and out of these vesicles. Immunofluorescence experiments on fixed GV and MII oocytes with antibodies to ZIP6, ZIP10 and ZnT3[20] revealed a cortical staining pattern at the plasma membrane for ZIP6 and ZIP10 but not for ZnT3 (data not shown, ZIP6 and ZIP10 data were recently published in Kong et al.[14]). The localization and relative number of ZincBY-1-stained compartments at the GV and MII stages are strikingly similar to a known vesicular cohort in eggs, the cortical granules (CGs). Cortical granules are Golgi-derived vesicles that are distributed throughout the oocyte cortex during oogenesis.[41,42] Cortical granule exocytosis occurs at the time of fertilization, resulting in the release of enzymes that modify the zona pellucida (ZP) and aid in the block to polyspermy.[43,44] To compare the distribution of the zinc-enriched structures to that of CGs, cells were fixed and stained for CGs following live cell labile zinc imaging at various stages during meiotic maturation (Figure 2). As the detection of labile zinc requires live cell imaging and the detection of CGs

requires fixation, we could not investigate their co-localization simultaneously in the same cell. Nevertheless, the sequential staining procedure demonstrated that the distribution of labile zinc (Figure 2b-i–v) was similar to cortical granule distribution (Figure 2b-vi–x). This co-localization was particularly striking at Anaphase I (AI), when both labile zinc and CGs were concentrated at the cleavage furrow. These data suggest that the zinc-enriched structures may be the same vesicles as or comprise a subpopulation of the CGs.

Ultrastructural elemental mapping corroborates the presence of cortical zinc-rich vesicular structures

To further examine whether ZincBY-1-labeled sites were in fact zinc-rich vesicles, we developed, optimized, and used a suite of elemental mapping approaches for the direct detection of zinc in subcellular compartments (STEM-EDS, Bionanoprobe XFM, and XFM tomography). With STEM-EDS, images with high spatial resolution (<10 nm) can be acquired that provide information about cellular structure and elemental content. However, elemental content is difficult to quantify using this technique. Bionanoprobe XFM complements STEM-EDS by enabling acquisition of images with good spatial resolution (<100 nm) and quantitative information about elemental content. Cellular structures, however, cannot be precisely visualized. XFM tomography allows us to further explore zinc distribution in these large cells by providing three-dimensional elemental information.

Traditional elemental mapping approaches require the use of sample fixation and embedding which is known to lead to metal ion loss.[45] Thus, we developed a new technique for detecting zinc in fixed samples based on the first step of the Timm silver staining method (autometallography).[46,47] In traditional Timm staining, biological samples are treated with a sulfide source to precipitate out highly insoluble metal sulfides, including zinc sulfide (ZnS, $K_{sp} = 4 \times 10^{-26}$ M^2),[48] and precipitation is followed by silver enhancement. The resulting electron-dense silver granules provide an indirect indication of pools of zinc ions (see supplementary information, Figure S6). However the size of the granules is a function of silver reduction conditions and does not accurately reflect the size of the biological compartment. To address these possible artifacts we eliminated the silver enhancement step and optimized the hydrogen sulfide treatment protocol for egg analysis. Briefly, whole freshly fixed cells are treated with 20 mM hydrogen sulfide/bisulfide solutions at neutral pH under conditions that stabilize Zn^{2+} ions in the form of ZnS; these samples can then be processed for elemental mapping (Figure 3a).

While sulfide treatment will not precipitate sulfides of more abundant cellular metals such as calcium (K_{sp} (CaS) = 8×10^{-7} M^2), it can also fix any weakly bound copper (K_{sp} (CuS) = 5×10^{-41} M^2, K_{sp} (Cu_2S) = 4×10^{-53} M^3) or iron stores (K_{sp} (FeS) = 1×10^{-21} M^2).[48] To directly resolve the identity of the metal we determined the spatially resolved x-ray fluorescence spectroscopic signatures of individual sulfide-fixed compartments using two distinct approaches, namely STEM-EDS and XFM using a high-resolution nanoprobe.

First, the elemental content of individual compartments in MII eggs was determined at the ultra-structural level using a Scanning Transmission Electron Microscope (STEM) designed with enhanced dual detectors for energy dispersive spectroscopy (EDS) (Figure 3b). The dual EDS detector design provides a nominal collection angle of 0.76 steradians, and thus

records much higher peak intensities compared to conventional single detector systems.[49] The multimodal capabilities of this instrument allow both anatomical and elemental imaging of samples, allowing us to push the boundaries of bioelemental imaging. Thin sections (200 nm) of a sulfide-fixed, resin-embedded MII egg were prepared, and imaged and analyzed by STEM for cellular structure and elemental content. Bright, vesicular structures near the ooplasmic membrane are evident in the Z-contrast image (Figure 3c, Figure S7), indicative of high molecular-weight elements in these regions. These regions range from 180 to 375 nm in diameter with a d_{avg} = 260 ± 50 nm (n = 23, Figure 3d). EDS spectra measured in electron-dense regions and nearby cytoplasm revealed significant zinc signal intensity above background in electron-dense regions (Figure 3e). Elemental map analysis of raster scans of an egg section (Figure 3f) further indicates that zinc fixation gives tight zinc distributions that overlay with electron dense regions in the Z-contrast image. Furthermore, analysis of zinc-enriched structures reveals a Zn and S mole ratio of ~1, consistent with formation of nanocrystalline deposits of zinc sulfide as the major metal-sulfide species within distinct boundaries (Figure S8). This approach provides the first ultrastructural maps of zinc in cells at <10 nm resolution. The size, morphology, chemistry and physiology support the designation of these compartments as zinc-enriched cortical vesicles.

X-ray fluorescence bionanoprobe microscopy allows quantification of zinc in cortical compartments

To further test conclusions from ultrastructural mapping and to address the quantity of zinc in each structure we used a synchrotron-based x-ray fluorescence microscope (XFM) bionanoprobe designed for quantitative high-resolution elemental mapping of biological samples.[50] High-resolution XFM zinc maps of thin sections of sulfide-treated MII eggs also showed a dense array of zinc-enriched compartments at the cell cortex, consistent with live-cell fluorescence and STEM-EDS results (Figure 4a). We note that the Fe and Cu are not enriched near the plasma membrane. Quantification of zinc content in these regions allows for the determination of total zinc concentrations within vesicular stores. We found that these stores contained a range of [Zn] from ~0.05 to ~1.8 M per compartment which was fitted to a Lorentzian distribution with a median at [Zn] = 0.2 M (Figure 4b).

X-ray fluorescence tomography demonstrates that cortical vesicles enriched in total zinc are polarized in three-dimensional space

To examine how these zinc-enriched vesicles are arranged in the three-dimensional context of the MII egg, we mapped the elemental content of the MII egg using x-ray fluorescence tomography.[51,52] In this approach, XFM maps of zinc-fixed and resin embedded MII eggs were acquired at multiple rotation angles (Figures 4c,e, supplemental movie S1), providing an unprecedented three-dimensional view of total zinc distribution within an intact mammalian egg. The spatial distribution of total elemental zinc observed in tomographic maps of the MII egg shows a number of similarities to that seen using vital fluorescent probes in the live egg. First, the XFM zinc map at the 0° rotation angle reveals a punctate distribution of sulfide-fixed zinc stores (Figure 4c-i). These punctate zinc regions are localized within the cell, as they overlay with the S map, which highlights the total volume of the egg (Figure 4c-ii, 4c-iii). In addition, Cu and Fe maps (Figure 4c-iv,v) do not exhibit a punctate pattern within the egg cell proper, suggesting that zinc is the predominant metal

contained within the cortical compartments. The zinc signal is also hemispherical, mirroring labile zinc distribution revealed by live-cell fluorescence microscopy with ZincBY-1 (Figure 4c-i, Figure 4c-iv). This result is particularly striking as XFM directly measures X-ray photons emitted from zinc atoms whereas ZincBY-1 fluorescence is an indirect readout of the presence of labile zinc. We found that the total number of Zn atoms measured within the embedded egg at all rotation angles yielded an average of $5.9\pm0.2 \times 10^{10}$ zinc atoms (Figure 4d). This value is within two percent of previously quantified zinc data in non-embedded cells (5.8×10^{10} atoms[5]), indicating that sulfide treatment preserves native zinc content within the cell. Similarly, Fe and Cu contents are also preserved.[5] Additional zinc maps at different rotation angles (Figure 4e) reveal that punctate zinc signal is both hemispherical and cortical, providing support for the conclusion that ZincBY-1 staining in live MII eggs corresponds to discrete subcellular sites containing elevated levels of labile zinc relative to the cytosol (for entire set of projections and a comparison between tomography and live-cell fluorescence imaging, see Movie S1).

Compartmentalized zinc release upon activation accounts for the zinc spark

Our previous studies demonstrated that labile zinc is lost from the egg via zinc sparks.[6] To determine whether zinc sparks arise from coordinated release of zinc ions from the discrete cortical compartments described above, we analyzed the spatio-temporal course of ZincBY-1-stained compartments concurrently with an extracellular zinc probe (FluoZin-3) at the time of egg activation. To analyze zinc flux across the full surface of this large (d = 70–75 μm) cell with the temporal resolution to capture a zinc spark event (<10 sec per frame), we acquired z-stacks with 5-micron thick optical sections during parthenogenetic egg activation (Movie S2, Figure 5). In these time course experiments, intracellular and extracellular fluorescence derive from ZincBY-1 and FluoZin-3 respectively. Three-dimensional reconstruction of the optical sections (Figure 5a, Movie S2) revealed that zinc release into the medium occurs from multiple hot spots on the egg surface in the hemisphere that contains ZincBY-1-stained compartments. When the fluorescence intensities of intracellular zinc (pre-spark) and extracellular zinc (during spark) were plotted as a function of angle, we noted a strong correlation (Figure 5b, 5c). Regions with the highest intensities of extracellular fluorescence mapped to the hemisphere at the vegetal pole (270°), the same hemisphere that contains the highest intensity of intracellular fluorescence originating from zinc-rich vesicles. Similarly, the regions with the lowest zinc spark intensities mapped to the zinc vesicle free zone at the animal pole (90°, Figures 5c, S9). This geometric analysis strongly supports the hypothesis that exocytosis of zinc-rich secretory compartments proximal to the ooplasmic membrane of the egg are the source of the extracellular zinc spark.

Although the z-resolution used to capture the zinc spark in three dimensions was too low to track individual vesicles, we performed subsequent higher resolution imaging within a single optical section to enable vesicle tracking (Figure 5d,e, Movie S3). Prior to increases in extracellular fluorescence, ZincBY-1-labeled zinc-rich vesicles were visible at the cortex (Figure 5d-i). Following the zinc spark (Figure 5d-ii), the majority of compartmentalized, cortical zinc staining is lost (Figure 5d-iii). Normalized fluorescence traces demonstrate that loss of punctate zinc staining occurs concurrently with the increase in extracellular

fluorescence (Figure 5e). This clearly demonstrates that zinc-rich compartments are released by the cell during a zinc spark and are the source of exocytosed zinc. We note that some cortical staining remains after the zinc spark; this is not surprising as the egg releases between one and five sparks and thus will require additional vesicles for subsequent sparks to occur. These results are consistent with the observation that there was no bright, cortical ZincBY-1 staining observed in $SrCl_2$-activativated parthenotes (Figure 1c-vii,viii) relative to the GV oocyte (Figure 1c-i,ii) and the MII egg (Figure 1c-iv,v).

Discussion

Using complementary quantitative chemical approaches for mapping zinc at the single cell level, we have defined a new family of discrete zinc-enriched vesicles that participate in the zinc fluxes that are essential in two critical stages of formation of a new mammal, namely oocyte maturation and egg fertilization. Our development of a vital probe for labile zinc pools allows qualitative interrogation of zinc fluxes at lower probe incubation concentrations (i.e. 50 nM) than commercially available and published agents. We used this intracellular probe along with extracellular FluoZin-3 to observe in concert the intracellular and extracellular components of the zinc spark,[6] as the coordinated exocytosis of thousands of zinc-enriched vesicles from the egg cortex. The identity of sites delineated by this probe as zinc enriched vesicles was established using three different approaches that also allowed more extensive analysis of the zinc concentration in these compartments. Quantitative single cell analysis revealed that this exocytosis is a mechanism underlying previously discovered loss of zinc between the egg and early embryo stages.[5,6] Specifically, fertilization or activation of the MII egg causes a steady loss of total zinc content— dropping by ca. 10% in the first 2 hours after fertilization and by 20% (i.e. loosing ca. 1×10^{10} zinc atoms) within the first 6 hours after fertilization. This lower zinc concentration then persists through the two cell-embryo stage (Figure 6). Given that vesicle-derived zinc sparks are produced by the egg within the first few hours of activation, we hypothesized that the 10–20% loss of total zinc content observed during this time period was likely due to the quantitative loss of zinc ions contained in cortical zinc vesicles. Precedence for this model comes from a variety of specialized cell types, including certain glutamatergic neurons[19,20] and pancreatic β-islet cells,[18,22] in which zinc efflux is associated with zinc-rich secretory vesicles. However, studies of zinc compartments within these systems have been largely qualitative.

By applying a suite of single-cell quantitative analytical methods, we can account for this zinc flux during mammalian fertilization. Quantitative characterization of zinc-rich compartments allows a mass balance of changes in zinc compartmentalization at the time of egg activation. Based on the absolute vesicular zinc content, we can gauge the percent of total cellular zinc that is in cortical compartments (Figure S10, Table S3). We measured a total zinc concentration of 0.2 M within a vesicle (bionanoprobe XFM). We note that previous studies in hippocampal systems estimated a 300 μM concentration for labile zinc within secretory vesicles in mossy fiber boutons.[53] The concentration we determined in the context of the egg is orders of magnitude higher than what has previously been measured in other systems (Figure 4b). The 0.2 M value reported here for the mouse egg vesicles may have contributions from both labile and tightly bound zinc ions. Using an average radius of 130 nm per vesicle (obtained from STEM measurements, Figure 3d) and the 0.2 M average

zinc concentration per vesicle, we estimate that an individual compartment will contain ca. 1 × 10^6 zinc atoms. Given a total of approximately 8000 cortical zinc-rich compartments in the MII egg (live cell fluorescence microscopy, Figure 1c), we estimate that the sum total of zinc in all cortical compartments corresponds to ca. 8 × 10^9 zinc atoms, or ~15% of the total zinc content of an MII egg (Figure 6, further calculation details and error analysis are provided in the supplementary information Figure S10 and Table S3). This number lies well within the 10–20% loss of total zinc that is observed in the hours following fertilization as reported in the literature.[5,6] Taken together, the similarity between the number of compartmentalized zinc atoms (8 × 10^9) and the number of zinc atoms lost following fertilization (1 × 10^{10}) indicates that cortical zinc compartments in the egg drive the zinc decreases that are requisite during fertilization. These results demonstrate that the egg sequesters zinc at high concentrations in vesicles at the cortex and subsequently releases the content of these compartments at the time of egg activation.

These cortical zinc-rich vesicles released during egg activation have a number of potential functions during fertilization. We noted that the changes in distribution and quantity of these vesicles throughout maturation and activation mirror that of cortical granules. These secretory vesicles are released at fertilization and contain biochemical species including enzymes that modify the egg's zona pellucida and thus play a role in the block to polyspermy.[41,42] Intriguingly one of the known cortical granule proteins, the zinc metalloprotease ovastacin, has been shown to cleave the zona pellucida glycoprotein ZP2 in a key step of zona hardening and prevention of polyspermy.[43] Alternatively, zinc-released by the egg could act directly on sperm to alter their function given the importance of zinc in mammalian sperm physiology.[34,35,54,55] Thus metals released during the zinc spark and the cortical reaction may play a number of roles outside the cell.

This study lays the groundwork for understanding how zinc fluxes can regulate events in multiple biological systems beyond the egg. At fertilization, the egg exploits a precise machinery for lowering intracellular zinc, i.e. the coordinated exocytosis of zinc-rich vesicles. Having quantitatively identified a major zinc regulation pathway in the egg during fertilization, we now stand poised to understand how zinc partitions between permissive and instructive functions in the biology of cellular transitions during development and beyond.

Methods

This section describes key experiments; an extended experimental section is provided in the Supplementary Methods.

Synthesis of ZincBY-1

3-Chloro-5-methoxy-8-mesityl-BODIPY(1) (32 mg, 0.085 mmol) and N^1-(pyridin-2-yl)-N^2,N^2-bis(pyridin-2-ylmethyl)ethane-1,2-diamine(2) (57 mg, 0.17 mmol) were combined in 5 mL of dry CH_3CN in an oven dried Schlenk flask under N_2. The reaction was heated at 80 °C overnight. Following cooling and solvent removal, the product was purified by silica gel chromatography (0–5% CH_3OH in CH_2Cl_2) to yield the pure product as a dark pink residue (40 mg, 70% yield).^{1}H NMR ($CDCl_3$, 500 MHz): ∂ 8.51 (1H, m), 8.48 (2H, m), 7.62 (3H, dq, J = 2.0, 7.5 Hz), 7.53 (2H, d, J = 8.0 Hz), 7.37 (1H, d, J = 8.0 Hz), 7.15 (1H, m), 7.12

(2H, m), 6.89 (2H, s), 6.34 (1H, d, J = 4.5), 6.10 (1H, d, J = 4.0 Hz), 5.87 (1H, d, J = 4.5 Hz), 5.61 (1H, d, J = 4.0 Hz), 5.22 (2H, s), 3.96 (3H, s), 3.89 (4H, s), 3.86 (2H, m), 2.92 (2H, m), 2.33 (3H, s), 2.08 (6H, s). HR-ESI-MS MH^+ $C_{39}H_{41}BF_2N_7O^+$calc. 672.3428, found 672. 3432. NMR spectra were obtained on a Bruker Avance-III 500 MHz. High resolution mass spectrum was measured on an Agilent 6210 LC-TOF. Additional experimental details are provided in the Supplementary Methods.

Animals, cell collection and culture

GV-stage oocytes were isolated from cumulus–oocyte complexes (COCs) collected from the ovaries of sexually mature (6–10 weeks old) female CD-1 mice injected with 5 IU pregnant mare's serum gonadotropin (PMSG, Sigma-Aldrich) 48 h before sample collection. Collection was performed in Leibovitz's L-15 medium (Life Technologies) supplemented with 1% (v/v) FBS (Life Technologies) and 0.2 mM 3-isobutyl-1-methylxanthine (IBMX, Sigma-Aldrich). To collect MII-arrested eggs at the metaphase II (MII) stage, females were injected with 5 IU PMSG and then 5 IU human chorionic gonadotropin (hCG, Sigma-Aldrich) 46 h later. Eggs were isolated from the oviducts 14 h after administration of hCG. Cumulus cells were denuded using 0.3% (w/v) hyaluronidase. Parthenotes were obtained by activating MII eggs in 10 mM $SrCl_2$ in Ca-free KSOM (Millipore) for 3h at 37 °C in an atmosphere of 5% CO_2. Successfully activated cells were selected based on extrusion of the second polar body. Animals were treated in accord with the US National Institutes of Health Guide for the Care and Use of Laboratory Animals. Food and water were given ad libitum. The Northwestern University Institutional Animal Care and Use Committee (IACUC) approved all protocols.

Live cell confocal microscopy

Confocal microscopy was performed on a Leica SP5 resonant scanner confocal microscope (Biological Imaging Facility, Northwestern University) and a Zeiss LSM 510 Confocal Microscope (Quantitative Bioelemental Imaging Center, Northwestern University). Intracellular zinc was visualized using 50 nM ZincBY-1 and extracellular zinc was visualized using 50 μM FluoZin-3 (Life Technologies). DNA was visualized using 10 μg/mL Hoechst 33342. In figures, fluorescence images within the same panel were collected and displayed using the same parameters. In activation experiments, eggs were activated using 10 mM $SrCl_2$ in Ca-free KSOM (Millipore). Further experimental details are provided in the Supplementary Methods.

Zinc-fixation of MII eggs

Following collection of MII eggs, the cells were fixed in 4 % Paraformaldehyde in PBS for one hour in the fridge. After fixation, the eggs were transferred into methyl cellulose capillaries and transferred to solutions of NaHS in PBS (pH 7), or for controls, in PBS only at 4° C. NaHS solutions were prepared by dissolving Na_2S in PBS over ice and adjusting solution pH to 7 using concentrated HNO_3 immediately prior to use. After 30 minutes of NaHS treatment, the eggs in capillaries were dehydrated in 10%, 25%, 50%, 75%, 90%, and 2 × 100% ethanol for 15 minutes each on ice. The samples were infiltrated with a 1:1 mixture of Spurr resin (EMS) and ethanol for 2 hours, followed by pure Spurr resin overnight 4° C. The next day, samples were placed in fresh Spurr resin in flat embedding

molds and polymerized for 72 hours at 65° C. Ultrathin sections were obtained with a diamond knife (Diatome) in an ultramicrotome (UC7, Leica).

Scanning Transmission Electron Microscopy with Energy Dispersive Spectroscopy

Ultrathin sections of 200 nm nominal thickness were placed on molybdenum slot grids with a carbon coated Formvar support film (EMS) and observed unstained. The sections were observed and analyzed with a dual EDS (Energy Dispersive X-ray Spectroscopy) system in a Hitachi STEM HD2300A at 200 kV acceleration voltage, using a 75 μm Objective aperture and 691 pA probe current. The electron dose was about 8.77×10^3 electrons per nm^2 (per single frame, 45 frames were recorded) in the spectral imaging mode for elemental maps. Elemental ratios in ZnS crystals were determined by removing the background with a digital top hat filter and by using the Cliff-Lorimer matrix correction without absorption. All EDS data analyses were carried out with the NSS Noran System Seven 2.2 Software (Thermo Scientific). Image resolution was determined based on the dimensions of smallest recognizable areas in elemental maps that contain pixels with zinc specific signal.

Supplementary Material

Refer to Web version on PubMed Central for supplementary material.

Acknowledgements

The authors would like to thank members of the O'Halloran, Woodruff, and Dravid labs for scientific discussions and advice. We thank Eric W. Roth for the preparation of electron microscopy samples and Jae-Hoon Chung and Junjie Shangguan for help with chemical synthesis. Equipment and experimental guidance was provided by the following core facilities at Northwestern University: the Integrated Molecular Structure Education and Research Center, the Biological Imaging Facility, the Quantitative Bioelemental Imaging Center, the Electron Probe Instrumentation Core, and the Keck Biophysics Facility. This work was supported by a Medical Research Award from the W. M. Keck Foundation, a SPARK Award from the Chicago Biomedical Consortium, and the National Institutes of Health (P01 HD021921, GM38784, U54HD076188 and T32GM105538).

References

1. Berg JM, Shi Y. The galvanization of biology: a growing appreciation for the roles of zinc. Science. 1996; 271:1081–1085. [PubMed: 8599083]
2. Finney LA, O'Halloran TV. Transition metal speciation in the cell: insights from the chemistry of metal ion receptors. Science. 2003; 300:931–936. [PubMed: 12738850]
3. O'Halloran TV. Transition metals in control of gene expression. Science. 1993; 261:715–725. [PubMed: 8342038]
4. Maret W. Zinc Biochemistry: From a Single Zinc Enzyme to a Key Element of Life. Adv. Nutr. 2013; 4:82–91. [PubMed: 23319127]
5. Kim AM, Vogt S, O'Halloran TV, Woodruff TK. Zinc availability regulates exit from meiosis in maturing mammalian oocytes. Nat. Chem. Biol. 2010; 6:674–681. [PubMed: 20693991]
6. Kim AM, et al. Zinc sparks are triggered by fertilization and facilitate cell cycle resumption in mammalian eggs. ACS Chem. Biol. 2011; 6:716–723. [PubMed: 21526836]
7. Bernhardt ML, Kim AM, O'Halloran TV, Woodruff TK. Zinc requirement during meiosis I-meiosis II transition in mouse oocytes is independent of the MOS-MAPK pathway. Biol. Reprod. 2011; 84:526–536. [PubMed: 21076080]
8. Bernhardt ML, Kong BY, Kim AM, O'Halloran TV, Woodruff TK. A zinc-dependent mechanism regulates meiotic progression in mammalian oocytes. Biol. Reprod. 2012; 86:114. [PubMed: 22302686]

9. Kong BY, Bernhardt ML, Kim AM, O'Halloran TV, Woodruff TK. Zinc maintains prophase I arrest in mouse oocytes through regulation of the MOS-MAPK pathway. Biol. Reprod. 2012; 87(11):11–12. [PubMed: 22539682]
10. Suzuki T, Yoshida N, Suzuki E, Okuda E, Perry AC. Full-term mouse development by abolishing Zn2+-dependent metaphase II arrest without Ca2+ release. Development. 2010; 137:2659–2669. [PubMed: 20591924]
11. Tian X, Diaz FJ. Zinc depletion causes multiple defects in ovarian function during the periovulatory period in mice. Endocrinology. 2012; 153:873–886. [PubMed: 22147014]
12. Krauchunas, AR.; Wolfner, MF. Curr. Top. Dev. Biol. Wassarman Paul, M., editor. Vol. 102. Academic Press; 2013. p. 267-292.
13. Suzuki T, et al. Mouse Emi2 as a distinctive regulatory hub in second meiotic metaphase. Development. 2010; 137:3281–3291. [PubMed: 20724447]
14. Kong BY, et al. Maternally-derived zinc transporters ZIP6 and ZIP10 drive the mammalian oocyte-to-egg transition. Mol. Hum. Reprod. 2014 in press.
15. Catterall A. Structure and function of voltage-gated ion channels. Annu. Rev. Biochem. 1995; 64:493–531. [PubMed: 7574491]
16. Cousins RJ, Liuzzi JP, Lichten LA. Mammalian zinc transport, trafficking, and signals. J. Biol. Chem. 2006; 281:24085–24089. [PubMed: 16793761]
17. Kühlbrandt W. Biology, structure and mechanism of P-type ATPases. Nat. Rev. Mol. Cell Biol. 2004; 5:282–295. [PubMed: 15071553]
18. Chimienti F, Devergnas S, Favier A, Seve M. Identification and cloning of a beta-cell-specific zinc transporter, ZnT-8, localized into insulin secretory granules. Diabetes. 2004; 53:2330–2337. [PubMed: 15331542]
19. Frederickson CJ, Suh SW, Silva D, Frederickson CJ, Thompson RB. Importance of zinc in the central nervous system: the zinc-containing neuron. J. Nutr. 2000; 130:1471S–1483S. [PubMed: 10801962]
20. Palmiter RD, Cole TB, Quaife CJ, Findley SD. ZnT-3, a putative transporter of zinc into synaptic vesicles. Proc. Natl. Acad. Sci. U.S.A. 1996; 93:14934–14939. [PubMed: 8962159]
21. Yamasaki S, et al. Zinc is a novel intracellular second messenger. J. Cell Biol. 2007; 177:637–645. [PubMed: 17502426]
22. Zalewski PD, et al. Video image analysis of labile zinc in viable pancreatic islet cells using a specific fluorescent probe for zinc. J. Histochem. Cytochem. 1994; 42:877–884. [PubMed: 8014471]
23. Fierke CA, Thompson RB. Fluorescence-based biosensing of zinc using carbonic anhydrase. Biometals. 2001; 14:205–222. [PubMed: 11831457]
24. Palmer AE, Qin Y, Park JG, McCombs JE. Design and application of genetically encoded biosensors. Trends Biotechnol. 2011; 29:144–152. [PubMed: 21251723]
25. Que EL, Domaille DW, Chang CJ. Metals in neurobiology: probing their chemistry and biology with molecular imaging. Chem. Rev. 2008; 108:1517–1549. [PubMed: 18426241]
26. Tomat E, Lippard SJ. Imaging mobile zinc in biology. Curr. Opin. Chem. Biol. 2010; 14:225–230. [PubMed: 20097117]
27. Fahrni CJ, O'Halloran TV. Aqueous Coordination Chemistry of Quinoline-Based Fluorescence Probes for the Biological Chemistry of Zinc. J. Am. Chem. Soc. 1999; 121:11448–11458.
28. Cork R. Problems with the application of quin-2-AM to measuring cytoplasmic free calcium in plant cells. Plant, Cell Environ. 1986; 9:157–161.
29. Laha JK, Dhanalekshmi S, Taniguchi M, Ambroise A, Lindsey JS. A Scalable Synthesis of Meso-Substituted Dipyrromethanes. Org. Proc. Res. Devel. 2003; 7:799–812.
30. Domaille DW, Zeng L, Chang CJ. Visualizing ascorbate-triggered release of labile copper within living cells using a ratiometric fluorescent sensor. J. Am. Chem. Soc. 2010; 132:1194–1195. [PubMed: 20052977]
31. Hureau C, et al. Syntheses, X-ray Structures, Solid State High-Field Electron Paramagnetic Resonance, and Density-Functional Theory Investigations on Chloro and Aqua MnII Mononuclear

Complexes with Amino-Pyridine Pentadentate Ligands. Inorg. Chem. 2008; 47:9238–9247. [PubMed: 18817370]

32. Ambundo EA, et al. Influence of Coordination Geometry upon CoppeRII/I) Redox Potentials. Physical Parameters for Twelve Copper Tripodal Ligand Complexes. Inorg. Chem. 1999; 38:4233–4242.
33. Rae TD, Schmidt PJ, Pufahl RA, Culotta VC, O'Halloran TV. Undetectable intracellular free copper: the requirement of a copper chaperone for superoxide dismutase. Science. 1999; 284:805–808. [PubMed: 10221913]
34. Andrews JC, Nolan JP, Hammerstedt RH, Bavister BD. Role of zinc during hamster sperm capacitation. Biol. Reprod. 1994; 51:1238–1247. [PubMed: 7888501]
35. Stoltenberg M, et al. Autometallographic demonstration of zinc ions in rat sperm cells. Mol. Hum. Reprod. 1997; 3:763–767. [PubMed: 9358001]
36. Zalewski P, et al. Use of a zinc fluorophore to measure labile pools of zinc in body fluids and cell-conditioned media. Biotechniques. 2006; 40:509. [PubMed: 16629398]
37. Outten CE, O'Halloran TV. Femtomolar sensitivity of metalloregulatory proteins controlling zinc homeostasis. Science. 2001; 292:2488–2492. [PubMed: 11397910]
38. Fahrni CJ. Synthetic fluorescent probes for monovalent copper. Curr. Opin. Chem. Biol. 2013
39. Gee KR, Zhou ZL, Qian WJ, Kennedy R. Detection and imaging of zinc secretion from pancreatic beta-cells using a new fluorescent zinc indicator. J. Am. Chem. Soc. 2002; 124:776–778. [PubMed: 11817952]
40. Burdette SC, Frederickson CJ, Bu W, Lippard SJ. ZP4, an improved neuronal Zn2+ sensor of the Zinpyr family. J. Am. Chem. Soc. 2003; 125:1778–1787. [PubMed: 12580603]
41. Ducibella T, Anderson E, Albertini DF, Aalberg J, Rangarajan S. Quantitative studies of changes in cortical granule number and distribution in the mouse oocyte during meiotic maturation. Dev. Biol. 1988; 130:184–197. [PubMed: 3141231]
42. Wessel GM, et al. The biology of cortical granules. Int. Rev. Cytol. 2001; 209:117–206. [PubMed: 11580200]
43. Burkart AD, Xiong B, Baibakov B, Jimenez-Movilla M, Dean J. Ovastacin, a cortical granule protease, cleaves ZP2 in the zona pellucida to prevent polyspermy. J. Cell Biol. 2012; 197:37–44. [PubMed: 22472438]
44. Tahara M, et al. Dynamics of cortical granule exocytosis at fertilization in living mouse eggs. Am. J. Physiol. 1996; 270:C1354–C1361. [PubMed: 8967435]
45. Stika KM, Bielat KL, Morrison GH. Diffusible ion localization by ion microscopy: a comparison of chemically prepared and fast-frozen, freeze-dried, unfixed liver sections. J. Microsc. 1980; 118:409–420. [PubMed: 7392047]
46. Timm F. Histochemistry of heavy metals; the sulfide-silver procedure. Dtsch Z. Gesamte Gerichtl Med. 1958; 46:706–711. [PubMed: 13597613]
47. Danscher G, Stoltenberg M, Bruhn M, Sondergaard C, Jensen D. Immersion autometallography: histochemical in situ capturing of zinc ions in catalytic zinc-sulfur nanocrystals. J. Histochem. Cytochem. 2004; 52:1619–1625. [PubMed: 15557216]
48. Licht S. Aqueous Solubilities, Solubility Products and Standard Oxidation-Reduction Potentials of the Metal Sulfides. J. Electrochem. Soc. 1988; 135:2971–2975.
49. Wu JS, et al. Imaging and elemental mapping of biological specimens with a dual-EDS dedicated scanning transmission electron microscope. Ultramicroscopy. 2013; 128:24–31. [PubMed: 23500508]
50. Chen S, et al. The Bionanoprobe: hard X-ray fluorescence nanoprobe with cryogenic capabilities. J. Synchrotron Radiat. 2014; 21:66–75. [PubMed: 24365918]
51. Hong YP, et al. Alignment of low-dose X-ray fluorescence tomography images using differential phase contrast. J. Synchrotron Radiat. 2014; 21:229–234. [PubMed: 24365941]
52. Gleber, S-C. J. Phys: Conf. Series. IOP Publishing; 012005
53. Frederickson CJ, Klitenick MA, Manton WI, Kirkpatrick JB. Cytoarchitectonic distribution of zinc in the hippocampus of man and the rat. Brain Res. 1983; 273:335–339. [PubMed: 6616240]

54. Foresta C, et al. Role of zinc trafficking in male fertility: from germ to sperm. Hum. Reprod. 2014; 29:1134–1145. [PubMed: 24771000]

55. Lishko PV, Kirichok Y. The role of Hv1 and CatSper channels in sperm activation. J. Physiol. 2010; 588:4667–4672. [PubMed: 20679352]

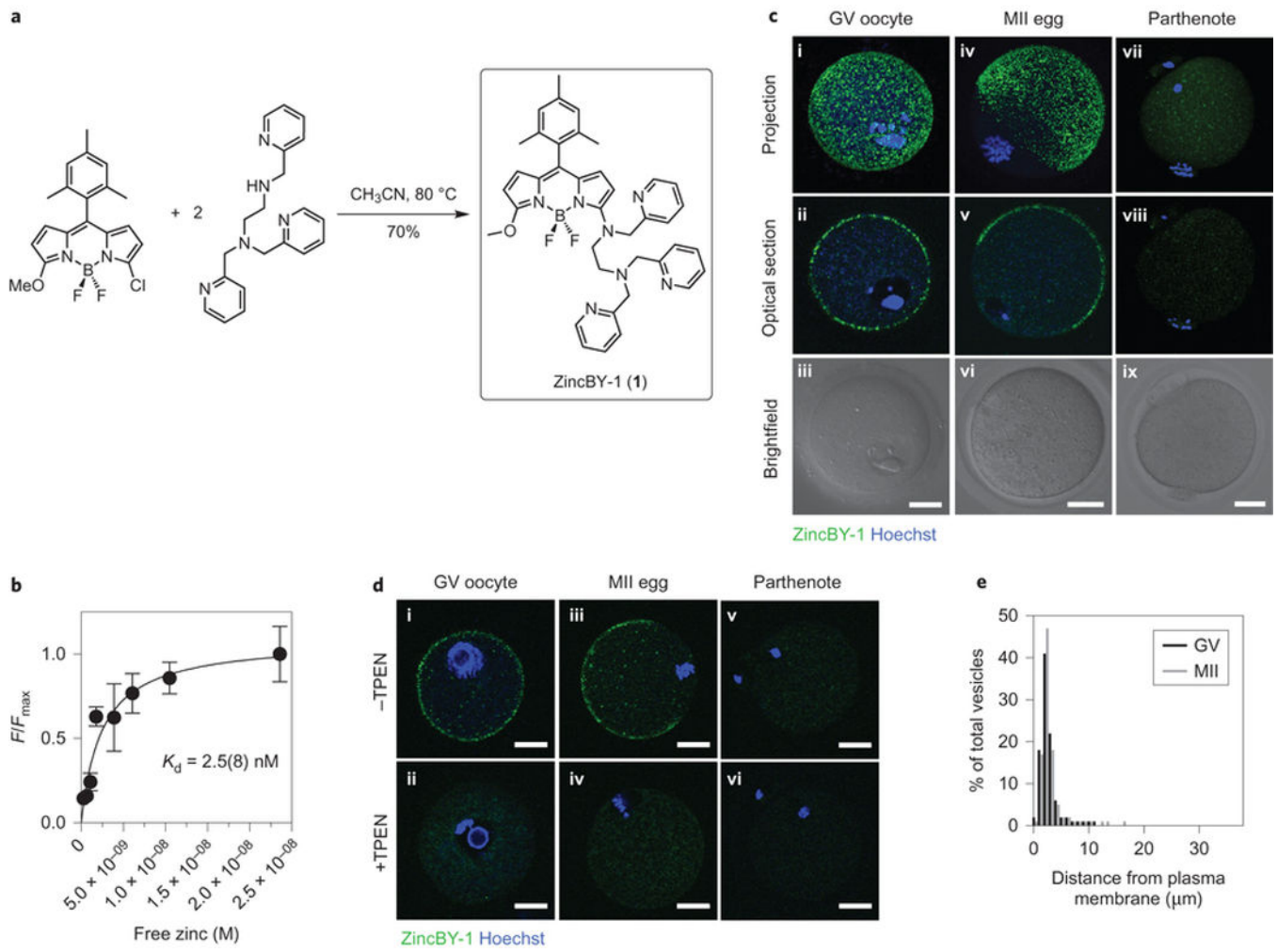

Figure 1. Vital zinc probe reveals cortical compartments in the female gamete in mouse

(a) Final step (see methods) in the synthesis of ZincBY-1, a novel fluorescent zinc probe.

(b) Fluorescence emission of ZincBY-1 in EGTA (ethylene glycol-bis(2-aminoethylether)-*N*,*N*,*N*′,*N*′-tetraacetic acid)-buffered Zn^{2+} solutions. Error bars represent ± S.E.M. (standard error of the mean). Spectra acquired in 100 mM KNO_3, 50 mM HEPES, pH 7.2, λ_{ex} = 520 nm. Integrated emission (530–700 nm) plotted vs. calculated [Zn^{2+}_{free}] and fitted to apparent K_d = 2.5 nM.

(c) GV (germinal vesicle) oocyte, MII (metaphase II) egg, and parthenote incubated with 50 nM ZincBY-1 (green) and DNA probe Hoechst 33342 (blue). Representative Z-stack projection (i, iv, vii), confocal optical slice (ii, v, viii), and brightfield (iii, vi, ix) images shown. Bright, punctate, cortical fluorescence from ZincBY-1 is observed in GV and MII cells.

(d) Incubation with 10 μM TPEN (N,N,N′,N′-tetrakis(2-pyridylmethyl)ethylenediamine) for 10 minutes abolishes cortical fluorescence in ZincBY-1 stained cells.

(e) Distance of ZincBY-1 compartments from the plasma membrane in GV (black) and MII (grey) cells. Vesicle positions sorted into 1 μm bins and plotted as a histogram. >90% of compartments are within 5 μm of the membrane in both cell types.

All scale bars = 20 μm

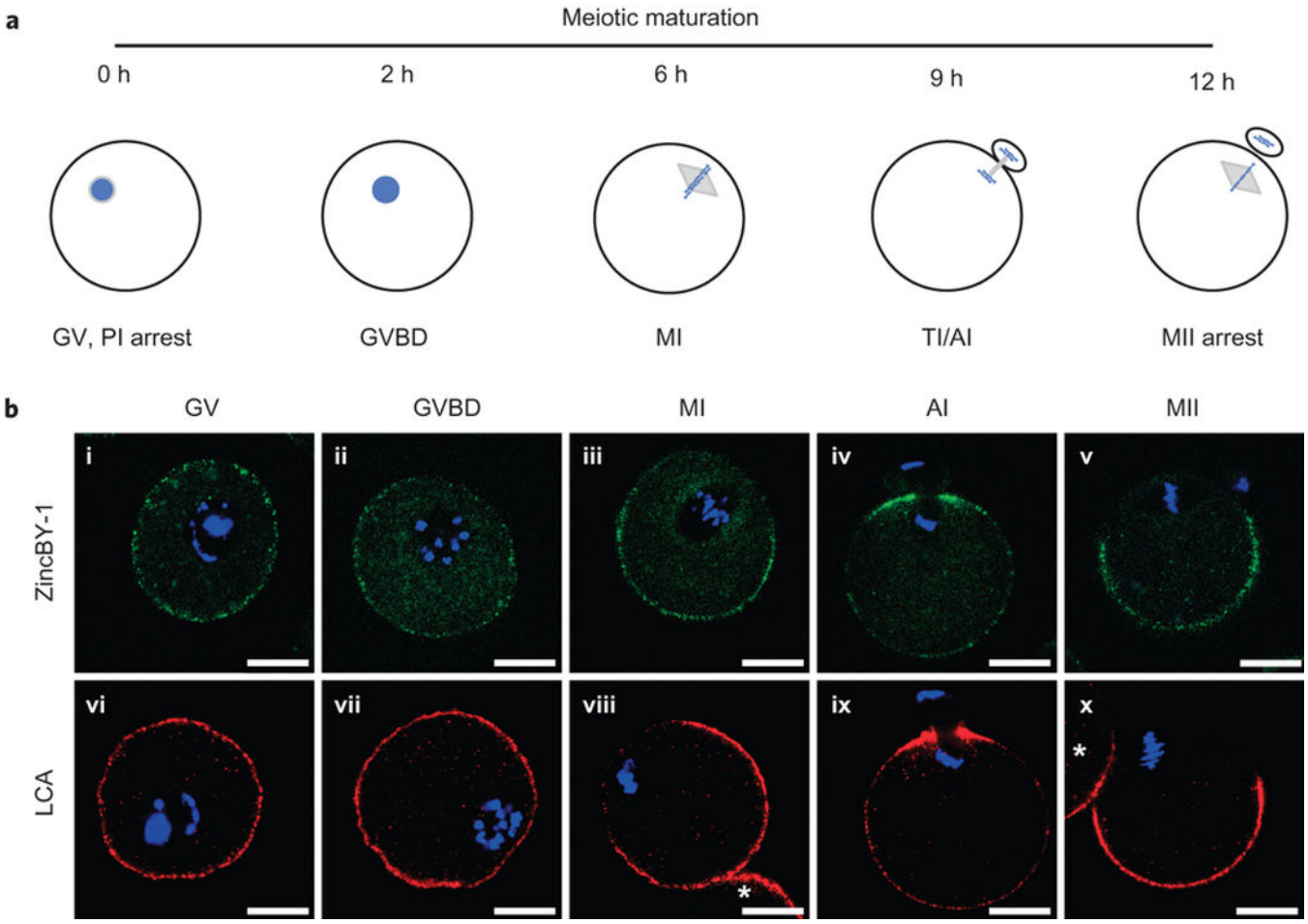

Figure 2. Labile zinc is cortically localized in the oocyte and tracks with cortical granule staining

(a) Schematic of meiotic maturation. GV oocytes in the ovary are arrested at prophase I (PI) of meiosis. Upon hormonal signaling, maturation begins and the cell progresses through meiosis until it arrests at metaphase II (MII), at which point the egg is competent for fertilization. Intervening stages during maturation include germinal vesicle breakdown (GVBD), metaphase I (MI) and Telophase I/Anaphase I (TI/AI).

(b) (i–v) Samples at GV, GVBD, MI, AI, MII were labeled with the zinc-specific probe ZincBY-1 (50 nM, green) to track labile zinc and counterstained with Hoechst 33342 to label DNA (blue).

(vi–x) Following zinc imaging, cells were fixed and stained for cortical granules using fluorescently labeled Lens culinaris agglutinin (LCA, red) and counterstained for DNA with DAPI (blue). Staining patterns for zinc and LCA are similar at each stage of maturation, suggesting that zinc-enriched structures may represent the same vesicles as, or comprise a subpopulation of the cortical granules. Representative optical confocal sections for each meiotic stage is shown. At least five oocytes were visualized at each stage in three independent experiments. Scale bars = 25 μm. * represents an adjacent oocyte.

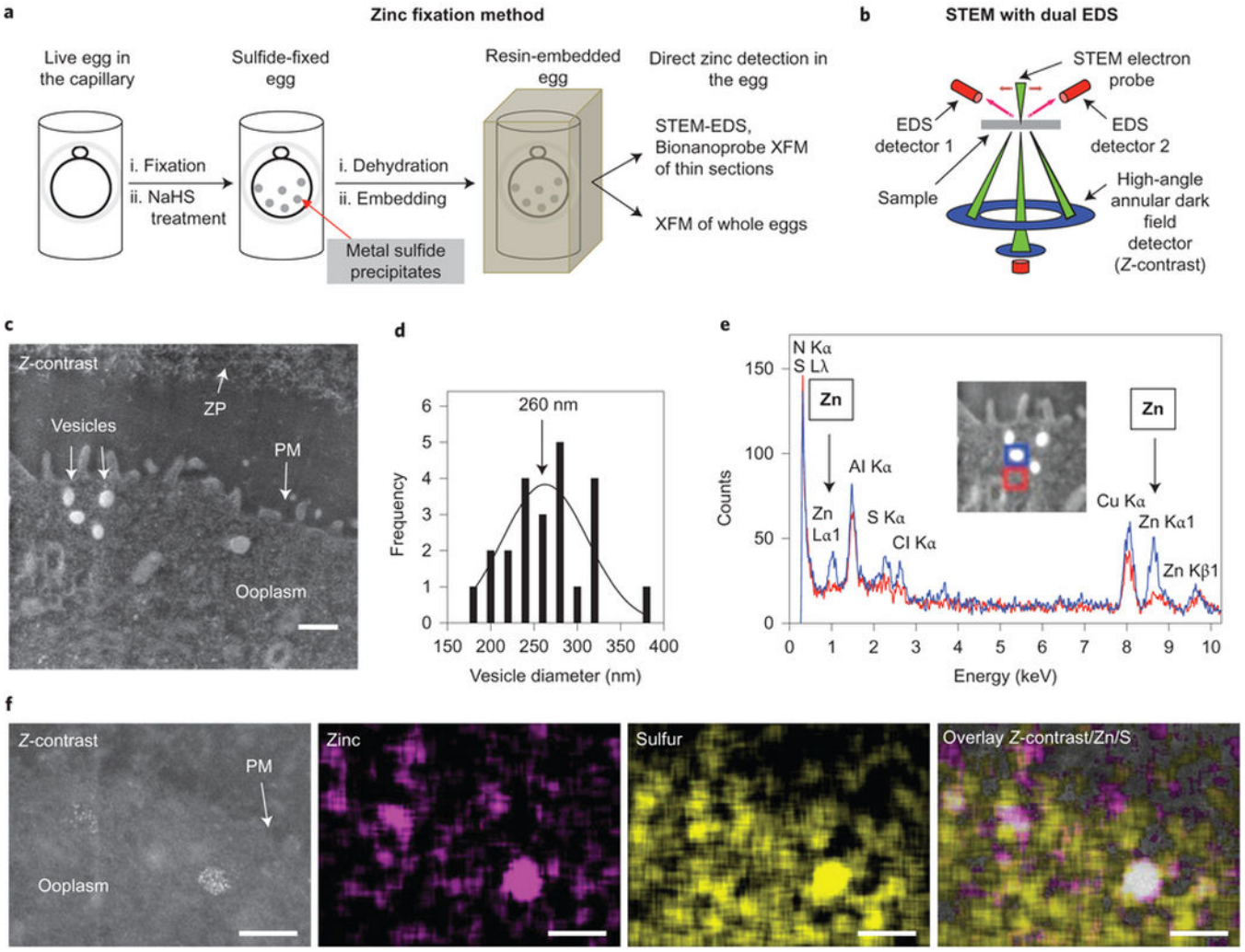

Figure 3. Zinc fixation enables ultrastructural identification of zinc-enriched cortical compartments by Scanning Transmission Electron Microscopy with Energy Dispersive Spectroscopy (STEM-EDS)

(a) Zinc-fixation schematic. Eggs were fixed and treated with NaHS to form ZnS. Following ethanol dehydration and resin embedding, eggs were used intact for X-ray fluorescence (XFM) tomography or sectioned prior to STEM-EDS or XFM Bionanoprobe analysis.

(b) Diagram of STEM microscope with dual EDS detectors for zinc mapping.[49]

(c) Z-contrast image of a 200 nm section of a resin-embedded MII egg following zinc fixation. Vesicles, zona pellucida (ZP), plasma membrane (PM) and ooplasm indicated. Bright and dark areas indicate regions with high and low molecular weight content respectively. Bright signal is concentrated in cortical compartments. Scale bar = 0.5 μm.

(d) Histogram of diameters of cortical compartments in STEM-EDS samples (20 nm bins). Distribution centers on a diameter of ~260 nm. Data from 23 Zn-enriched compartments from 8 eggs.

(e) EDS spectra of bright compartment (blue) and cytoplasm (red). Zinc signal is enriched in the compartment relative to the cytoplasm.

(f) Z-contrast, Zn and S EDS maps of a cortical region in a MII egg. Overlay demonstrates that Zn-rich regions correspond to areas high in S and electron density (Z-contrast).

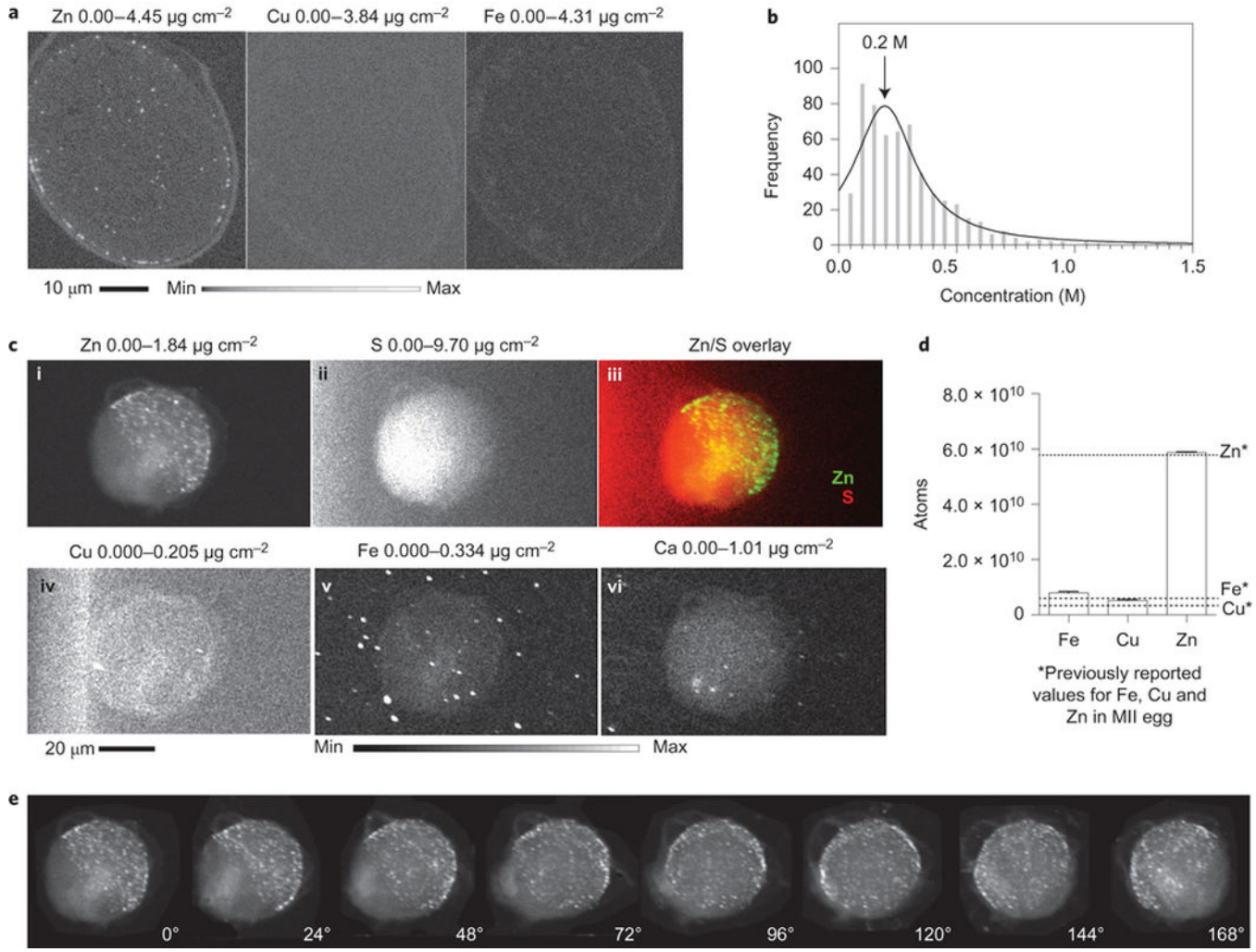

Figure 4. X-ray fluorescence microscopy and tomography provides zinc quantification and mapping within the egg

(a) Bionanoprobe XFM images of a 400 nm thick egg section. Zn, Cu, and Fe maps shown with concentration ranges. Scale bar = 10 μm, pixels = 100 × 100 nm^2. High [Zn] observed in punctate cortical structures.

(b) Histogram of [Zn] in punctate regions (bins = 0.05 M). Data fitted to a Lorentzian distribution (black line) centered on [Zn] = 0.2 M.

(c) XFM tomography images at 0° angle of intact MII egg following zinc fixation. Zn (i), S (ii), Cu (iv), Fe (v), and Ca (vi) maps shown with concentration ranges. Zn/S map overlay (iii) demonstrates zinc-rich regions are intracellular. Scale bar = 20 μm.

(d) Total metal content quantification in resin-embedded MII egg following zinc fixation. Bars represent average number of atoms over 60 projection images of the same sample (Fe = 8±4 × 10^9; Cu = 5±3 × 10^9; Zn = 6±2 × 10^{10}). Error bars represent ± S.E.M. Dashed lines represent previously measured values in unfixed eggs.[5] Results indicate that this zinc fixation protocol preserves total Zn content.

(e) Zn maps at several angles (° indicated) illustrate a cortical, hemispherical distribution of Zn-enriched regions.

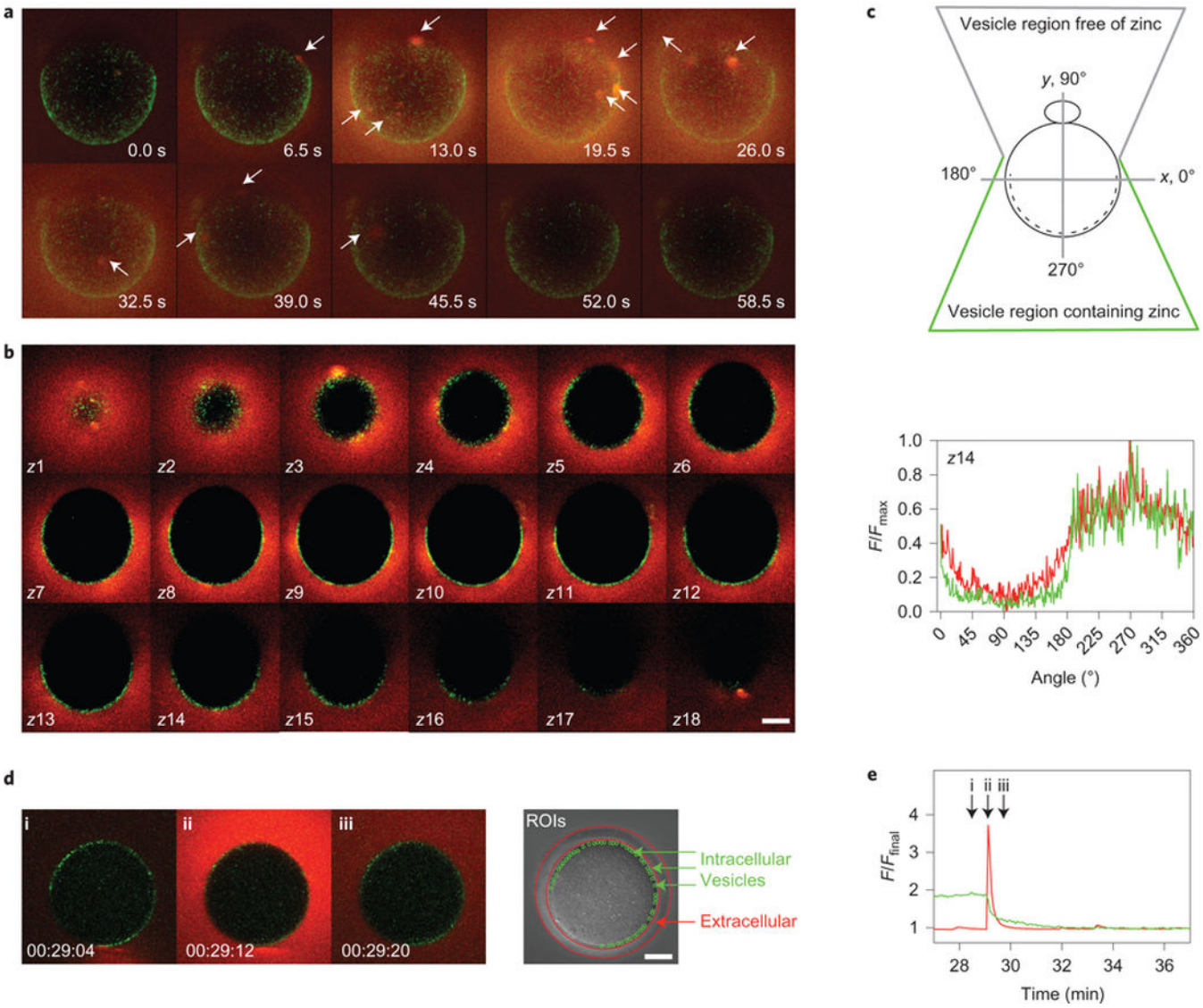

Figure 5. Live cell fluorescence zinc imaging demonstrates intracellular zinc compartments are the source of the extracellular zinc spark

MII eggs labeled with 50 nM ZincBY-1 (intracellular, green) were activated with 10 mM $SrCl_2$ in medium containing 50 μM FluoZin-3 (extracellular, red). All scale bars = 20 μm.

(a–c) Whole egg was imaged in a z-stack time course (5 μm optical sections taken over 6.5 seconds).

(a) Z-stack projections of ZincBY-1 and FluoZin-3 fluorescence during a zinc spark. Arrows indicate concentrated regions of zinc exocytosis.

(b) Overlaid optical sections of pre-spark ZincBY-1 fluorescence and FluoZin-3 fluorescence during a zinc spark. Z-stack position is indicated in each panel.

(c) Angular analysis of intracellular and extracellular fluorescence distribution in a z-section (z14 shown, others in SI). Fluorescence intensity pattern is the same in both channels, indicating that zinc-enriched vesicles are the source of the zinc spark.

(d–e) Egg imaged in a 1 μm confocal section.

(d) Images from time course taken before (i), during (ii), and after (iii) a zinc spark. Brightfield image indicates intracellular and extracellular ROIs.
(e) Time traces show simultaneous decrease in intracellular fluorescence and increase in extracellular fluorescence, indicating that zinc-enriched vesicles are the source of the zinc spark.

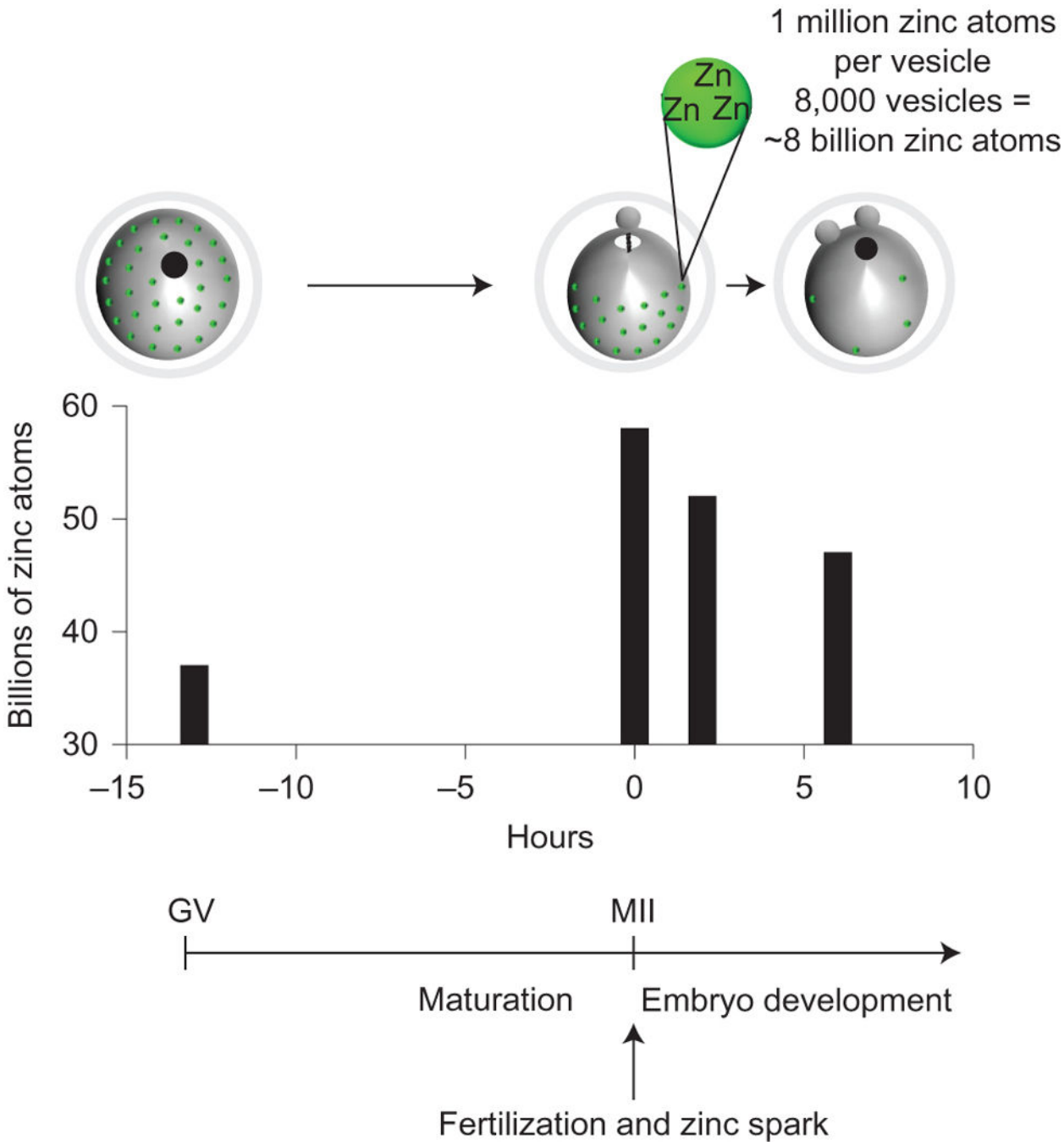

Figure 6. The zinc flux during egg activation is regulated by a quantitative loss of cortical zinc compartments

This schematic diagram summarizes the fluxes in total zinc that are observed during maturation and immediately following fertilization/egg activation. The meiotic cycle in the mammalian egg occurs over a very short period of time that is accompanied by a very large flux in the amount and localization of the inorganic element zinc (black bars).[5,6] Through the combined used of our novel zinc probe ZincBY-1 for live cell imaging and a suite of fixed cell imaging technologies (sulfide-zinc fixation, STEM-EDS, Bionanoprobe XFM, XFM tomography), we have estimated that there are 8,000 zinc-enriched cortical vesicles in

the egg, each containing ~1 million zinc atoms. These vesicles, containing in total 8 billion zinc atoms, are lost at fertilization during the zinc spark and quantitatively contribute to zinc efflux that is required during the egg-to-embryo transition. This study sets a precedent for how zinc can be quantitatively tracked during key biological processes.